4D Flow MRI-Based Pressure Loss Estimation in Stenotic Flows: Evaluation Using Numerical Simulations

Belén Casas Garcia, Jonas Lantz, Petter Dyverfeldt and Tino Ebbers

Linköping University Post Print

N.B.: When citing this work, cite the original article.

Original Publication:

Belén Casas Garcia, Jonas Lantz, Petter Dyverfeldt and Tino Ebbers, 4D Flow MRI-Based Pressure Loss Estimation in Stenotic Flows: Evaluation Using Numerical Simulations, 2016, Magnetic Resonance in Medicine, (75), 4, 1808-1821.
http://dx.doi.org/10.1002/mrm.25772

Copyright: 2015 The Authors. Magnetic Resonance in Medicine published by Wiley Periodicals, Inc. on behalf of International Society for Magnetic Resonance in Medicine. This is an open access article under the terms of the Creative Commons Attribution-NonCommercial-NoDerivs License.
http://eu.wiley.com/WileyCDA/

Postprint available at: Linköping University Electronic Press
http://urn.kb.se/resolve?urn=urn:nbn:se:liu:diva-127426

4D Flow MRI-Based Pressure Loss Estimation in Stenotic Flows: Evaluation Using Numerical Simulations

Belen Casas,[1,2]* Jonas Lantz,[1,2,3] Petter Dyverfeldt,[1,2] and Tino Ebbers[1,2,3]

Purpose: To assess how 4D flow MRI-based pressure and energy loss estimates correspond to net transstenotic pressure gradients (TPG_{net}) and their dependence on spatial resolution.

Methods: Numerical velocity data of stenotic flow were obtained from computational fluid dynamics (CFD) simulations in geometries with varying stenosis degrees, poststenotic diameters and flow rates. MRI measurements were simulated at different spatial resolutions. The simplified and extended Bernoulli equations, Pressure-Poisson equation (PPE), and integration of turbulent kinetic energy (TKE) and viscous dissipation were compared against the true TPG_{net}.

Results: The simplified Bernoulli equation overestimated the true TPG_{net} (8.74 ± 0.67 versus 6.76 ± 0.54 mmHg). The extended Bernoulli equation performed better (6.57 ± 0.53 mmHg), although errors remained at low TPG_{net}. TPG_{net} estimations using the PPE were always close to zero. Total TKE and viscous dissipation correlated strongly with TPG_{net} for each geometry ($r^2 > 0.93$) and moderately considering all geometries ($r^2 = 0.756$ and $r^2 = 0.776$, respectively). TKE estimates were accurate and minorly impacted by resolution. Viscous dissipation was overall underestimated and resolution dependent.

Conclusion: Several parameters overestimate or are not linearly related to TPG_{net} and/or depend on spatial resolution. Considering idealized axisymmetric geometries and in absence of noise, TPG_{net} was best estimated using the extended Bernoulli equation. **Magn Reson Med 75:1808–1821, 2016. © 2015 The Authors. Magnetic Resonance in Medicine published by Wiley Periodicals, Inc. on behalf of International Society for Magnetic Resonance.**

Key words: pressure loss; phase contrast magnetic resonance imaging; aortic valve disease; aortic coarctation

INTRODUCTION

The transstenotic pressure gradient is an important parameter in the assessment of the severity of valvular and vascular diseases such as aortic stenosis and aortic coarctation. The net transstenotic gradient determines the ventricular workload required to maintain a certain arterial pressure, and thereby reflects the hemodynamic significance of the stenosis. This parameter has shown to be a good predictor of adverse clinical outcome in patients with aortic stenosis (1). Cardiac catheterization is considered the gold standard for measuring pressure gradients, but the use of this procedure is limited due to its invasiveness.

In the clinical setting, ultrasonography is the primary noninvasive method for evaluating transstenotic pressure gradients. The maximum transstenotic pressure gradient (TPG_{max}) is estimated from the simplified Bernoulli equation using Doppler measurements of the velocity at the vena contracta (2). However, this approximation is known to overestimate the actual pressure gradient, referred to as net transstenotic pressure gradient (irreversible pressure drop, TPG_{net}). The main reason for this discrepancy is the pressure recovery phenomenon, characterized by reconversion of a certain amount of kinetic energy into pressure downstream from the stenosis (3–10). The amount of kinetic energy that is not converted back to pressure is lost as a result of conversion into thermal and acoustic energy. This amount is relatively small in laminar flow, but increases drastically under turbulent conditions. In the simplified Bernoulli equation, pressure recovery is assumed to be negligible.

Improved noninvasive estimation of TPG_{net} can be obtained from TPG_{max} by introducing a correction factor to account for pressure recovery. This correction factor often involves noninvasive measurements of parameters reflecting the geometry of the stenosis and the outflow tract. Garcia et al, for example, derived a modification of the simplified Bernoulli equation that takes the ratio between the effective orifice area and the cross sectional area of the aorta into account (1).

Pressure differences can also be computed from three-directional three-dimensional cine phase-contrast MRI (4D flow MRI) velocity data. Using the MRI velocities as an input, the Navier-Stokes equations provide the gradients of the pressure field under laminar flow conditions. Relative pressure maps can then be obtained by integration of the computed gradients, normally by solving the Pressure Poisson equation (PPE) (11,12).

More recently, new research directions have focused on defining alternate metrics to quantify irreversible energy losses directly from 4D flow MRI measurements. Dyverfeldt et al proposed volumetric integration of the turbulent kinetic energy (TKE) in the poststenotic region

---

[1] Division of Cardiovascular Medicine, Department of Medical and Health Sciences, Linköping University, Linköping, Sweden.

[2] Center for Medical Image Science and Visualization (CMIV), Linköping University, Linköping, Sweden.

[3] Division of Media and Information Technology, Department of Science and Technology/Swedish e-Science Research Centre (SeRC), Linköping University, Linköping, Sweden

Grant sponsor: European Research Council; Grant number: 310612; Grant sponsor: Swedish Research Council.

*Correspondence to: Belen Casas, M.Sc., KVM, Department of Medical and Health Sciences, Linköping University, SE-581 83 Linköping, Sweden. E-mail: belen.casas.garcia@liu.se

Received 2 December 2014; revised 7 April 2015; accepted 23 April 2015
DOI 10.1002/mrm.25772

Published online 28 May 2015 in Wiley Online Library (wileyonlinelibrary.com).

© 2015 The Authors. Magnetic Resonance in Medicine published by Wiley Periodicals, Inc. on behalf of International Society for Magnetic Resonance in Medicine. This is an open access article under the terms of the Creative Commons Attribution-NonCommercial-NoDerivs License, which permits use and distribution in any medium, provided the original work is properly cited, the use is non-commercial and no modifications or adaptations are made.

© 2015 Wiley Periodicals, Inc.

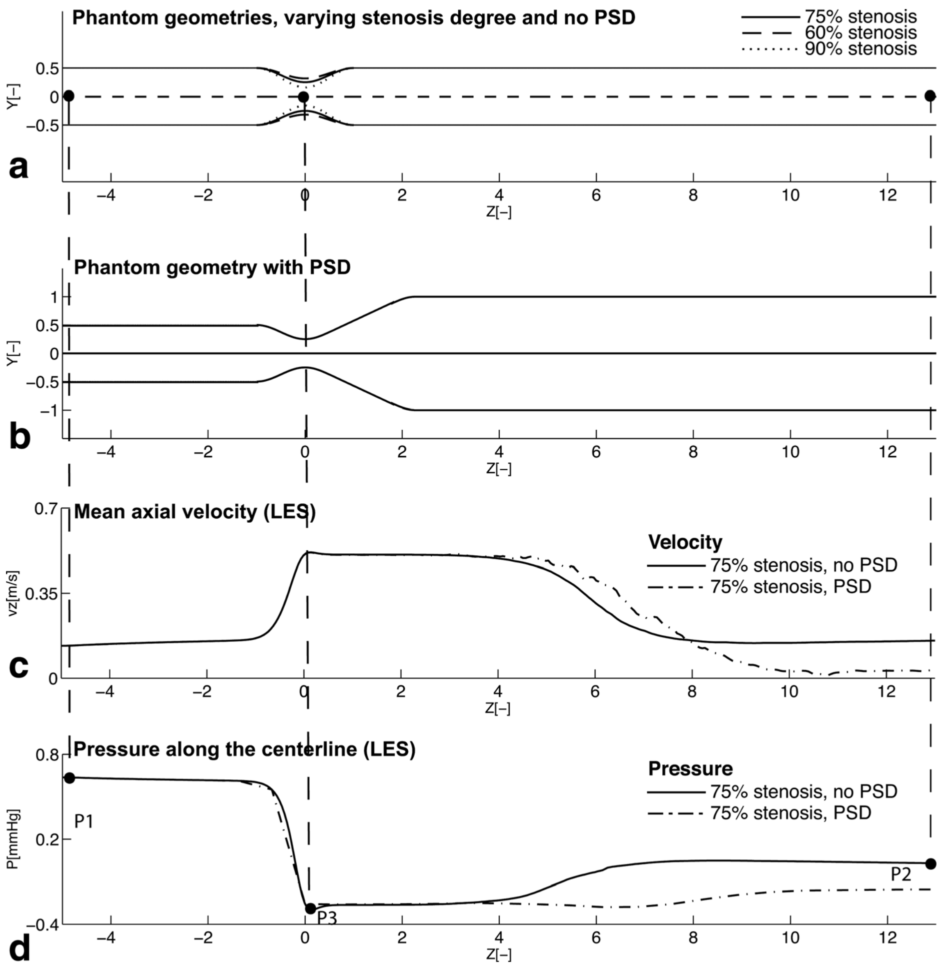

FIG. 1. Schematic of the numerical flow phantoms. **a**: Phantom with 60% (dashed line), 75% (solid line) and 90% (dotted line) stenosis area reduction. **b**: Phantom with 75% stenosis area reduction and poststenotic dilation (PSD) with diameter twice the upstream diameter. Z and Y represent the distance from the center of the stenosis, normalized by the upstream diameter (14.6 mm). The main flow direction is in the positive Z direction. Note that the length of the geometry shown here is limited to 13 unconstricted diameters from the center of the stenosis, 21 diameters were used in the LES computations. **c**: Mean velocity in the axial direction (v_z) along the centerline of the phantom for geometries with 75% stenosis and Reynolds number 2000, without poststenotic dilation (solid line) and with poststenotic dilation with diameter 2·D (dash dotted line). **d**: The corresponding pressures (P) along the centerline of the phantom for these geometries and flow settings are presented. Axial velocity and pressure were obtained from the LES solution.

as a potential way to estimate TPG_{net} (13), given that the primary cause of energy loss in stenotic flow is turbulence dissipation into heat (14). TKE can be measured with data obtained from a conventional 4D flow MRI acquisition (15). Alternatively, energy losses in completely nonturbulent flows can be estimated by the viscous dissipation (16), a parameter that can also be derived from 4D flow MRI velocity data.

Although a wide range of options for the assessment of stenosis severity has been proposed and applied in studies of different pathologies (17–20), the correspondence between the derived pressure and energy loss parameters and the actual net transstenotic pressure gradient is unclear. This may partly be due to the lack of reference pressure measurements in many studies. Rather than using catheters, in vivo comparisons are often performed against estimations of TPG_{max} or TPG_{net} that can be obtained noninvasively (1). For instance, Bock et al (18) calculated pressure differences in aortic coarctation patients based on the PPE and found a moderate underestimation ($14.7\% \pm 15.5\%$) when comparing with maximum pressure gradients from the simplified Bernoulli equation. Dyverfeldt et al found a strong linear relationship ($r^2 = 0.91$) between the total TKE and a pressure loss index in patients with aortic stenosis (13). A strong linear relationship ($r^2 = 0.91$) was also found between the viscous energy loss dissipation term and an estimation of TPG_{net} in healthy volunteers and patients with aortic dilation and stenosis for a wide range of pressure gradients (0–60 mmHg) (16).

Spatial resolution may be critical in computing some of these parameters, as stenotic blood flow is dominated by high jet velocities and strong gradients at the jet boundary. These strong gradients can only be computed accurately when the spatial resolution is sufficient. Nasiraei-Moghaddam et al (21) investigated the accuracy of pressure estimations from phase-contrast (PC) -MRI data using the PPE in a stenotic flow phantom by

Table 1
Geometries, flow settings and PC-MRI simulation settings considered in the study

Geometry		Reynolds number (Re)[b]	TPG_{net} (mmHg)	VENC (m/s)
Stenosis	∅ PSD[a]			
60%	-	1000	0.05	0.1
60%	-	2000	0.16	0.15
75%	-	1000	0.15	0.15
75%	-	2000	0.58	0.4
75%	-	3000	1.23	0.5
75%	-	4000	2.32	0.7
75%	-	5000	3.70	1
75%	-	6000	5.26	1
90%	-	500	0.32	0.2
90%	-	2000	4.78	1
90%	-	3000	10.74	1.5
90%	-	4000	19.14	2
90%	-	5000	29.02	2.5
90%	-	6000	40.44	4
75%	2·D	1000	0.21	0.1
75%	2·D	2000	0.77	0.2
75%	2·D	3000	1.66	0.3
75%	2·D	4000	3.07	0.5
75%	2·D	5000	4.78	0.7
75%	2·D	6000	6.79	1

[a] Diameter of the poststenotic dilation, defined in relation to the upstream diameter D (14.6 mm).

[b] $Re = \rho v D/\mu$, where ρ is the fluid density, v and D the velocity and diameter at the inlet, respectively, and μ the dynamic viscosity of the fluid.

comparison with pressure obtained from computational fluid dynamics (CFD) simulations of the same geometry. They found that the accuracy of the estimations was affected by both the spatial resolution and the presence of turbulence, and reported errors up to 6.9% in the estimated pressure drop. This study, however, was limited to low Reynolds numbers (< 540), which are not fully representative of the range of stenosis found in patients with aortic disease. Similarly, Venkatachari et al (22) investigated the impact of resolution in the computation of viscous dissipation through a series of in vitro experiments in a U-shaped phantom under laminar flow conditions, and reported that high spatial resolution is required. In their study, for a flow rate of 1.2 L/min, the percentage error between the viscous dissipation obtained from CFD data and the PC-MRI estimations using in-plane resolutions of 1×1 and 0.6×0.6 mm^2 was 30.5 and 2.4%, respectively.

The purpose of this study was to evaluate the ability of current 4D flow MR-based pressure and energy loss estimations to predict TPG_{net} within a clinically relevant range of stenosis severity. Additionally, we sought to assess the impact of spatial resolution in these estimations.

METHODS

Time-resolved data of nonpulsatile turbulent flow were obtained using CFD simulations in a stenotic geometry at different flow rates and degrees of stenosis. MRI measurements were simulated from the numerical flow data for different spatial resolutions. Three methods for the estimation of pressure gradients were implemented: the simplified Bernoulli equation, the extended Bernoulli equation and the Pressure-Poisson equation. Irreversible energy losses were estimated using two parameters: total TKE and viscous dissipation. The relationship between the calculated parameters and the true net transstenotic pressure gradient, obtained directly from the CFD solution, was assessed using linear regression.

Numerical Model

The geometry consisted of a rigid pipe with an unconstricted diameter of 14.6 mm and a cosine-shaped stenosis (23,24) that had a cross-sectional area reduction of 60, 75, and 90%. In addition, a geometry with a 75% stenosis and a poststenotic dilatation (PSD) with a diameter of two times the upstream diameter (14.6 mm) was investigated. The range of geometries included in the study is shown in Figure 1.

Nonpulsatile flow was simulated numerically by solving the Navier-Stokes equations in ANSYS CFX 14.5. The computational meshes were made in ANSYS ICEM 14.5 and consisted of high quality anisotropic hexahedral cells. The amount of cells was on the order of 10–18 million, depending of Reynolds number (Re) (25–28). The nondimensional wall distance y+ was always less than unity to ensure a good near-wall resolution, as this is required to resolve the near wall turbulent flow features correctly (25–28). The thickness of the mesh cells close to the wall grew exponentially by a factor of 1.05 until it matched the mesh size in the center of the stenosis.

Turbulent flow fluctuations were resolved using Large Eddy Simulation (LES), a technique that resolves the larger energy-carrying turbulent scales and models the smaller isotropic scales where energy dissipation occurs (25–28). The LES technique has been validated against both Laser Doppler Velocimetry and direct numerical simulations (26). The simulation used the WALE subgrid scale model (27), and the numerical schemes were second order accurate. The time step was 50 μs for the simulations with $Re < 4000$, and 25 μs for $Re = 5000$ and 6000, which has been shown to be sufficient for these kinds of flow (25–28). The convergence criteria was $1{\cdot}10^{-6}$and global imbalances of mass and momentum were always less than 0.1%, which ensured that the simulation was computed with sufficient accuracy (25–28). Sampling of flow statistics started after initial transient startup effects had disappeared (i.e., the standard deviation of the velocity signal was constant over 0.25 s), typically after 1 s flow time.

A fully developed velocity profile was set as inlet boundary condition, while a constant static pressure was set at the outlet. The inlet and outlet were placed 4 unconstricted diameters upstream and 21 downstream from the stenosis, respectively. The walls were considered rigid and to obey the no-slip condition. The fluid was water with a constant density of 997 kg/m^3 and dynamic viscosity of $8.899{\cdot}10^{-4}$ kg/(m·s).

Simulations were performed for Reynolds numbers in a range from 500 to 6000, resulting in TPG_{net} values of 6.76 ± 0.54 mmHg (range 0.05–40.4 mmHg) and TPG_{max} 8.63 ± 0.68 mmHg (range, 0.08–51.9 mmHg). The choice of phantom geometries, Reynolds numbers and the corresponding pressure gradients are summarized in Table 1.

PC-MRI simulations

The PC-MRI signal was simulated for all voxels within the volume, considering isotropic voxel sizes of 1, 1.5, and 2 mm. The velocity distributions $s(v_i)$ of the velocity components v_i in three perpendicular directions $(i = x, y, z)$ were obtained by estimating the probability density function of the velocities within the voxel, using a 3D Gaussian point spread function (PSF). In this way, the velocity of each cell j within the voxel was weighted with a coefficient w_j based on the cell's distance to the center of the voxel (29):

$$w_j = \frac{e^{-d_j^2/2\sigma^2}}{W} \quad [1]$$

where d_j is the distance of the j-th cell to the center of the voxel, W the sum of the weights within the voxel (i.e., $W = \sum_j w_j$) and σ the variance of the Gaussian function, defined from the isotropic spatial resolution Δz as $\sigma = \Delta z/2.35$ (30).

In simulating the PC-MRI mean velocity data, each voxel comprised time-averaged data from a converged LES solution. The mean velocity in each direction was computed as the average of the velocities within the voxel, taking into account the weights defined by the Gaussian PSF. Voxels at the centerline of the phantom comprised approximately 400 cells for 1 mm spatial resolution, while voxels located in the stenosis region and the proximity of the wall included a higher number of cells due to the increased density of the mesh at these locations. In simulating the PC-MRI data used for TKE calculations, each voxel comprised data from a converged LES solution with a separation of 20 ms between consecutive time steps (31). This represents the time difference between sampling of two phase-encoding lines in an interleaved 4D flow MRI acquisition with a 5 ms repetition time (TR). The number of time steps included varied between 20 and 29, depending on the expected amount of turbulence. The PC-MRI signal $S_i(k_v)$ for each direction i was computed as the Fourier transform of the velocity distribution $s(v_i)$, defined as $S_i(k_v) = \int_{-\infty}^{\infty} s(v_i) e^{-ik_v v_i} dv_i$, where $k_v (i.e.\ \pi/VENC)$ corresponds to the applied motion sensitivity. The intravoxel velocity standard deviation σ_i can then be derived from the magnitude relationship between the PC-MRI signals measured at two different motion sensitivities, assuming a Gaussian velocity distribution within the voxel (15). A nonsymmetric flow-encoding scheme was used to obtain measurements at zero motion sensitivity $(S_i(0))$ and motion sensitivity $k_v(S_i(k_v))$, allowing σ_i estimations as follows:

$$\sigma_i = \frac{1}{k_v}\sqrt{2\ln\left(\frac{|S_i(0)|}{|S_i(k_v)|}\right)}\ \left(\mathrm{ms}^{-1}\right). \quad [2]$$

Partial volume effects (i.e., the mixture of low and high velocity flow in the same voxel) result in mean velocity variations that contribute to the velocity distribution $s(v_i)$ and are, therefore, reflected in the estimations of the mean velocity and σ_i (31). Such effects are often present at the vessel boundary and the jet's periphery and result in elevated values of σ_i.

The simulations did not incorporate noise and saturation effects, and ideal bipolar gradients were considered. For each of the geometries and flow rates, k_v was adjusted to provide the maximum accuracy for σ_z, as given by: $k_v \cdot \sigma_z = 1$ (31). To calculate k_v, a prior estimation of σ_z was obtained by computing the standard deviation of the velocities within the voxel. The calculated VENC values are included in Table 1.

Parameter Computation

Simplified Bernoulli

The simplified Bernoulli equation, as applied clinically, was used according to Baumgartner et al (32):

$$\Delta P_{simpBernoulli} = 4v_{vc}^2(\mathrm{mmHg}) \quad [3]$$

where v_{vc} was defined as the velocity at the vena contracta. v_{vc} was calculated as the maximum velocity along the centerline of the phantom, obtained from the PC-MRI simulations of the mean velocity field. The expression in Eq. [3] is derived for blood, which has a density of $\rho = 1060\ Kg/m^3$. In this study, water was considered instead, thus Eq. [3] was modified to be applicable for water ($\rho = 997\ Kg/m^3$). All pressure values in the different methods are expressed in mmHg. The true value of $\Delta P_{simpBernoulli}$ was computed from the LES data to assess the dependence on resolution of the MR-based estimation. This dependence was evaluated for the different resolution settings, corresponding to voxel sizes of 1, 1.5, and 2 mm. The same resolution values were considered for all the methods in this study.

Extended Bernoulli

An extended version of the simplified Bernoulli equation, designed to take pressure recovery and the effect of the poststenotic geometry into account, was applied according to Keshavarz-Motamed et al (33):

$$\Delta P_{extBernoulli} = 4v_{vc}^2\left(1 - \frac{EOA}{A_A}\right)^2(\mathrm{mmHg}) \quad [4]$$

where EOA is the effective orifice area and A_A the area of the aorta. The value of EOA was obtained from the continuity equation under the assumption of a flat axial velocity profile, $A_p v_p = EOA v_{vc}$, where A_p was set to the cross-sectional area proximal to the stenosis and v_p to the maximum velocity in the cross section (32,34).

Pressure Poisson Equation (PPE)

The Navier-Stokes equations for an incompressible Newtonian fluid were used to calculate a pressure gradient field:

$$\nabla \boldsymbol{P} = -\rho\frac{\partial \boldsymbol{v}}{\partial t} - \rho\boldsymbol{v}\cdot\nabla\boldsymbol{v} + \mu\nabla^2\boldsymbol{v} + \boldsymbol{g} \quad [5]$$

where $\nabla \boldsymbol{P} = \left(\frac{\partial P}{\partial x}, \frac{\partial P}{\partial y}, \frac{\partial P}{\partial z}\right)$ is the three-directional pressure gradient and $\boldsymbol{v} = (v_x, v_y, v_z)$ the PC-MRI velocity field. As the flow is nonpulsatile, the transient inertia term $\frac{\partial \boldsymbol{v}}{\partial t}$

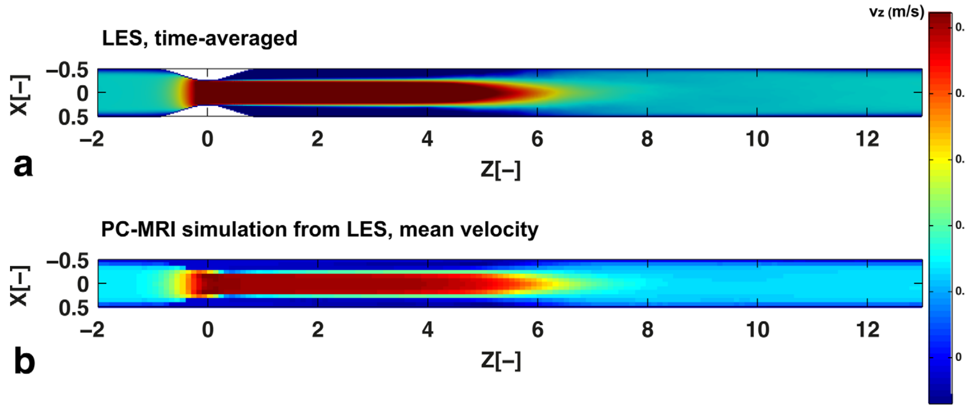

FIG. 2. The mean velocity in the axial direction (v_z) from the time averaged LES solution (**a**) and the PC-MRI simulation from the time averaged LES solution (**b**). Z and X show the distance from the center of the stenosis, normalized by the upstream diameter. The principal flow direction is in the positive Z direction. The simulation corresponds to a geometry with 75% stenosis degree and Re equal to 2000. The voxel size was set to 1 mm.

was omitted. The gravitational force $\boldsymbol{g}$ was disregarded. First order ($\nabla \boldsymbol{v}$) and second order ($\nabla^2 \boldsymbol{v}$) spatial derivatives of the velocity in each voxel were calculated by polynomial expansion (35), using normalized convolution to handle uncertainties in the boundaries of the volume of interest. The convolution kernel was defined as a three-dimensional Gaussian function with spatial size 5 voxels and variance 0.6.

From the estimated gradients, relative pressures were calculated by solving the PPE using a multigrid solver (11). Especially in a flow phantom, voxels located at the wall and the boundary of the jet exhibit large velocity gradients, mainly in the axial direction, due to partial volume effects. Our preliminary results indicated that such gradients reduced the accuracy of the solution. Therefore, similar to Riesenkampff et al (36), we did not include these voxels in the calculations as they were not critical in computing pressures along the centerline of the phantom. The computational domain was set to a rectangular volume containing the central part of the flow, approximately three voxels along the x and y directions for a 1 mm resolution.

A PPE-based estimate of the net transstenotic pressure gradient, ΔP_{PPEnet}, was obtained from the pressure at two points *P1* and *P2* along the centerline of the phantom, as illustrated in Figure 1. Additionally, the maximum pressure gradient $\Delta P_{PPE\max}$ was estimated considering the pressure at the center of the constriction (point *P3* in Figure 1).

Viscous Energy Loss

The viscous dissipation function ϕ_v per voxel was calculated from the first order spatial gradients of the simulated 3D mean velocity field:

$$\phi_v = \frac{1}{2}\sum_i \sum_j \left[\left(\frac{\partial v_i}{\partial x_j} + \frac{\partial v_j}{\partial x_i}\right) - \frac{2}{3}(\nabla \cdot \boldsymbol{v})\delta_{ij}\right]^2 \ \left(\mathrm{s}^{-2}\right) \qquad [6]$$

where i and j represent the perpendicular directions x, y z and δ_{ij} is the Kronecker delta (37). The rate of viscous dissipation $\dot{E}_{loss\ \ viscous}$ (i.e. energy loss rate) was then estimated by integration of the viscous dissipation function over the phantom volume, according to:

$$\dot{E}_{loss\ \ viscous} = \mu \sum_{i=1}^{Nvoxels} \phi_v V_i \ (\mathrm{W}) \qquad [7]$$

where μ is the viscosity, V_i is the volume of each individual voxel (m^3) and N_{voxels} the total number of voxels within the volume. $\dot{E}_{loss\ \ viscous}$ was also calculated as proposed by Barker et al (16), thus omitting dissipation near the wall. For each data set, voxels with viscous dissipation close to the wall were visually identified and excluded from the calculations. Similarly, $\dot{E}_{loss\ \ viscous}$ was computed from the high-resolution LES data for comparison against the MR-based estimates.

Total Turbulent Kinetic Energy

For each voxel in the volume, the TKE was computed from the intravoxel velocity standard deviation σ_i in each direction, according to Pope (38):

$$TKE = \frac{1}{2}\rho \sum_{i=1}^{3} \sigma_i^2 \ \left(\mathrm{Jm}^{-3}\right). \qquad [8]$$

The voxel-wise TKE was integrated in the entire phantom volume. The total TKE was also computed directly from the LES data for comparison against the MR-based estimates.

Statistical Analysis

Results are given as mean ± standard error unless otherwise stated. Simple linear regression was used to assess the relationship between the estimated parameters and the true $\mathrm{TPG}_{\mathrm{net}}$. For each parameter, regression analysis was performed for the complete $\mathrm{TPG}_{\mathrm{net}}$ interval and the coefficient of determination (r^2) was calculated. Additionally, the linear relationship between the energy loss parameters (viscous energy dissipation and total TKE) and $\mathrm{TPG}_{\mathrm{net}}$ was tested for each data subset corresponding to a specific geometry. A t-test was used

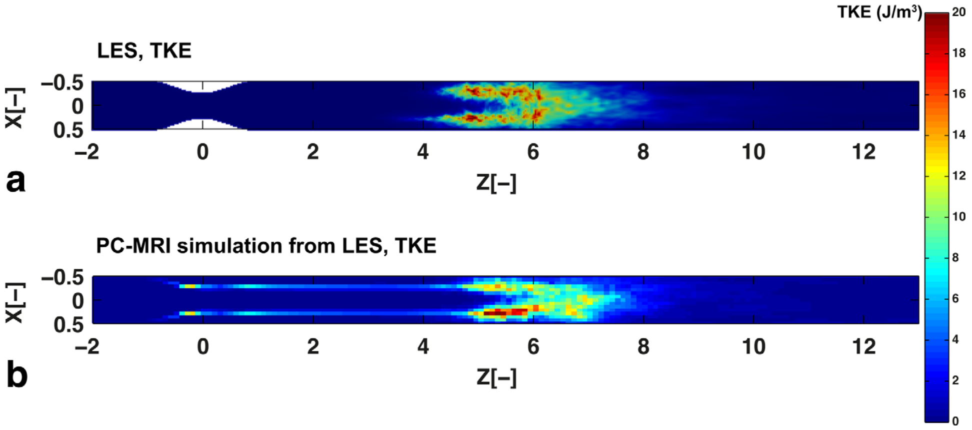

FIG. 3. The TKE computed from the LES data (**a**) and the PC-MRI simulation from the LES solution (**b**). Z and X show the distance from the center of the stenosis, normalized by the upstream diameter. The principal flow direction is in the positive Z direction. The simulation corresponds to a geometry with 75% stenosis degree and Re equal to 2000. The voxel size was set to 1 mm.

to test the null hypothesis that the slope of the regression line is equal to zero. Bland-Altman analysis was used to evaluate the agreement between the true TPG_{net} and the pressure estimations from the simplified Bernoulli equation, the extended Bernoulli equation and the PPE.

RESULTS

The mean velocity field in the axial direction obtained from the time averaged LES solution and the PC-MRI simulation for one of the geometries are shown in Figure 2. Figures 3 and 4 show comparisons between the TKE and viscous dissipation function as obtained from the MR-simulations and the corresponding values obtained from the LES data. The PC-MRI simulation and the LES solution agreed visually for both turbulence intensity and viscous dissipation, although viscous dissipation was overall underestimated in the PC-MRI simulation. Furthermore, partial volume effects were seen along the jet's periphery in both the TKE and the viscous energy dissipation maps. These effects are most pronounced in the vicinity of the stenosis, around $Z = 0$.

The pressure gradients estimated using the simplified Bernoulli equation ($\Delta P_{simpBernoulli}$) were 8.74 ± 0.67 mmHg. When compared with the true TPG_{net} (Fig. 5), the results of linear regression and Bland-Altman were $r^2 = 0.998$, slope of the regression line 1.242 ($P < 0.001$), bias = 1.979 mmHg and limits of agreement: −3.250 and 7.210 mmHg, indicating a very strong linear relationship but overestimation of the pressure gradients. The relative error (Fig. 5b) tended to be larger for low degrees of stenosis, and was related to the stenosis geometry. For similar values of TPG_{net} in the pressure range 0–15 mmHg, the relative error was higher for 60% stenosis and 75% stenosis without poststenotic dilation.

When the maximum pressure gradient was considered instead, the estimated gradients $\Delta P_{simpBernoulli}$ showed a very strong linear relationship ($r^2 = 0.999$) and were in close agreement with the values of TPG_{max} obtained from the CFD simulations (bias = 0.104 mmHg and agreement limits: −0.674 and 0.881 mmHg).

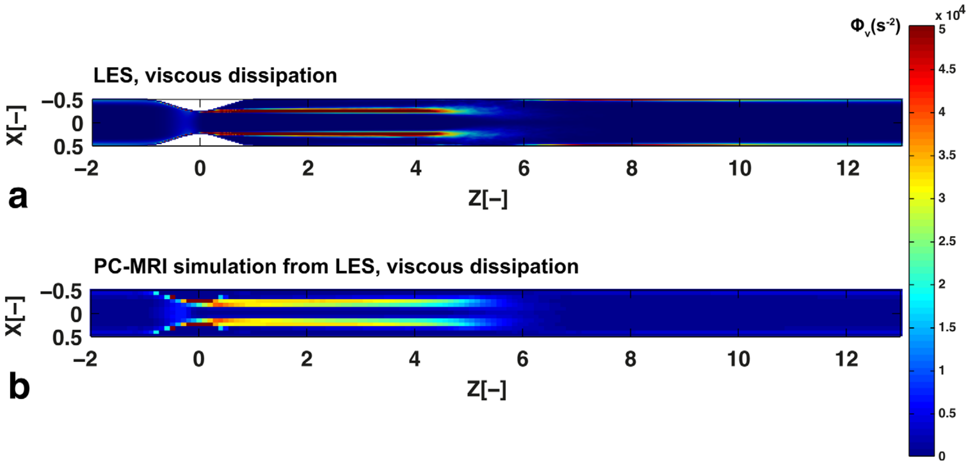

FIG. 4. The viscous dissipation function (ϕ_v) computed from the LES data (**a**) and the PC-MRI simulation from the LES solution (**b**). Z and X show the distance from the center of the stenosis, normalized by the upstream diameter. The principal flow direction is in the positive Z direction. The simulation corresponds to a geometry with 75% stenosis degree and Re equal to 2000. The voxel size was set to 1 mm.

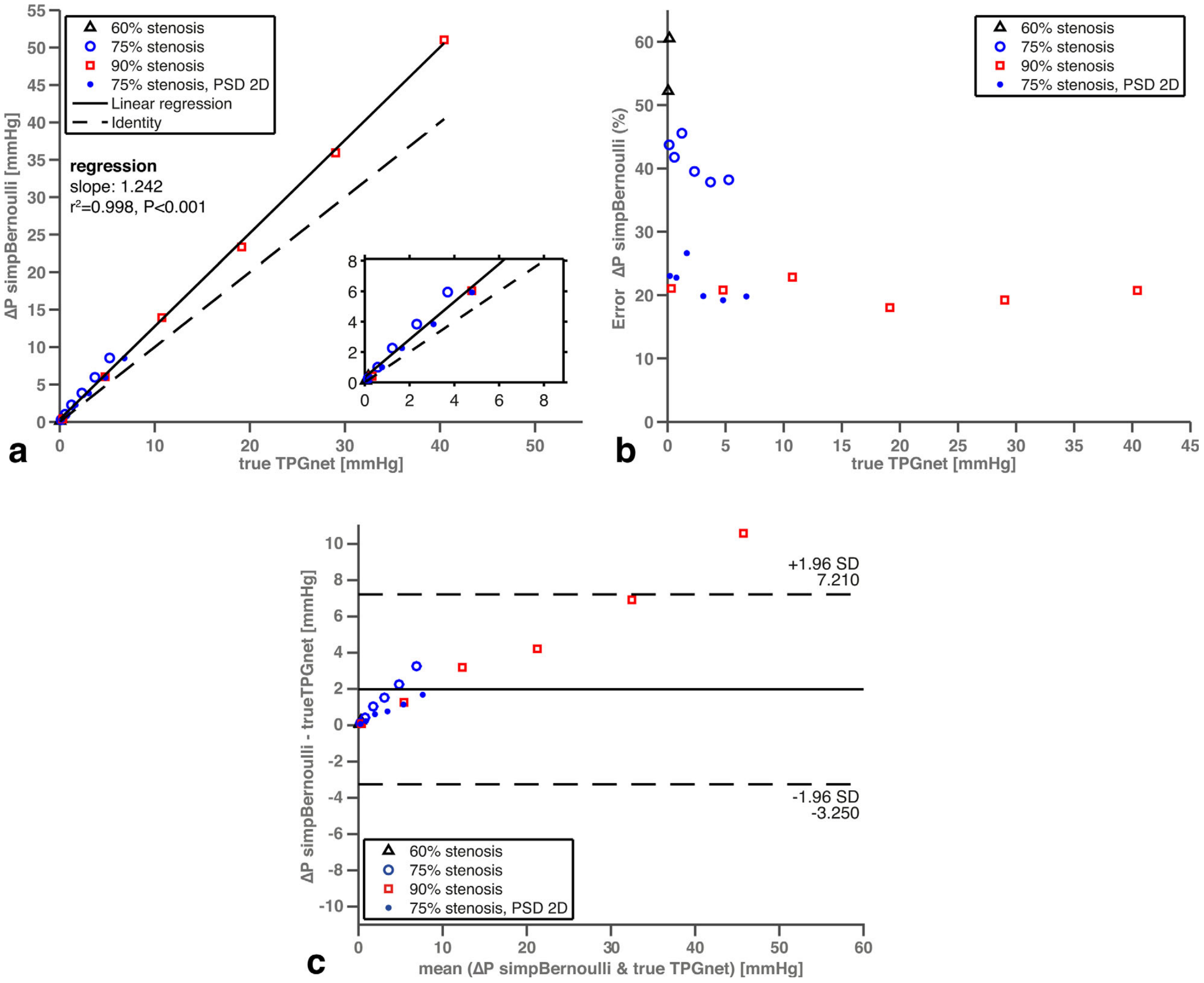

FIG. 5. Pressure gradient estimates using the simplified Bernoulli equation. **a**: Correlation between the estimated pressure gradient $\Delta P_{simpBernoulli}$ and the true TPG_{net}, obtained from the LES solution. The results correspond to an isotropic voxel size of 1 mm. The solid line represents the linear regression line and the dotted line the identity. The regression line was computed for the whole TPG_{net} interval. **b**: Percentage error between the estimated pressure gradient $\Delta P_{simpBernoulli}$ and the true TPG_{net}. **c**: Bland-Altman plot of $\Delta P_{simpBernoulli}$ versus true TPG_{net}. The solid line is the mean bias and the dashed lines represent the ± 1.96 standard deviation (SD) lines. The different symbols indicate different geometries (size of the stenosis and presence of poststenotic dilation). For a specific geometry, increasing pressure gradients correspond to increasing Reynolds numbers.

Estimations of the pressure gradient using the extended Bernoulli equation ($\Delta P_{extBernoulli}$) are shown in Figure 6. The estimated gradients were 6.57 ± 0.53 mmHg. A very strong linear relationship ($r^2 = 0.999$) and strong agreement (bias $= -0.188$ mmHg and limits of agreement: -0.987 and 0.610 mmHg) was found between $\Delta P_{extBernoulli}$ and the true TPG_{net}. The slope of the regression line was 0.980 ($P < 0.001$). Similar to the simplified Bernoulli equation, the method performed better for pressure values in the interval 15–40.4 mmHg. The relative error was also dependent on the geometry of the stenosis, and was also found to be higher for geometries with 60% and 75% stenotic area reduction (Fig. 6b). However, in contrast to the Bernoulli equation, the extended Bernoulli approach underestimated the pressure gradients for these geometries. The average differences between the pressure gradients computed from the LES data and the MRI estimations were highest for a voxel size of 2 mm, and were 0.86% for the simplified Bernoulli equation and 0.87% for the extended Bernoulli equation.

Figure 7 shows the estimations obtained from the PPE. The estimations of the net transstenotic pressure gradient, ΔP_{PPEnet}, showed a poor agreement with the true $TPG_{net.}$ (Fig. 7a). The slope of the regression line was -0.052, and the estimations were close to 0 for the whole pressure range (-0.45 ± 0.03 mmHg). When the maximum pressure gradient obtained from the PPE ($\Delta P_{PPE\max}$) was used as an estimation of TPG_{net}, the results of linear regression and Bland-Altman analysis (coefficient of determination $r^2 = 0.997$, slope of the regression line 1.188 ($P < 0.001$), bias $= 1.379$ mmHg and agreement limits: -2.787 and 5.545 mmHg) revealed an overestimation in the entire pressure interval (Figs. 7b,c).

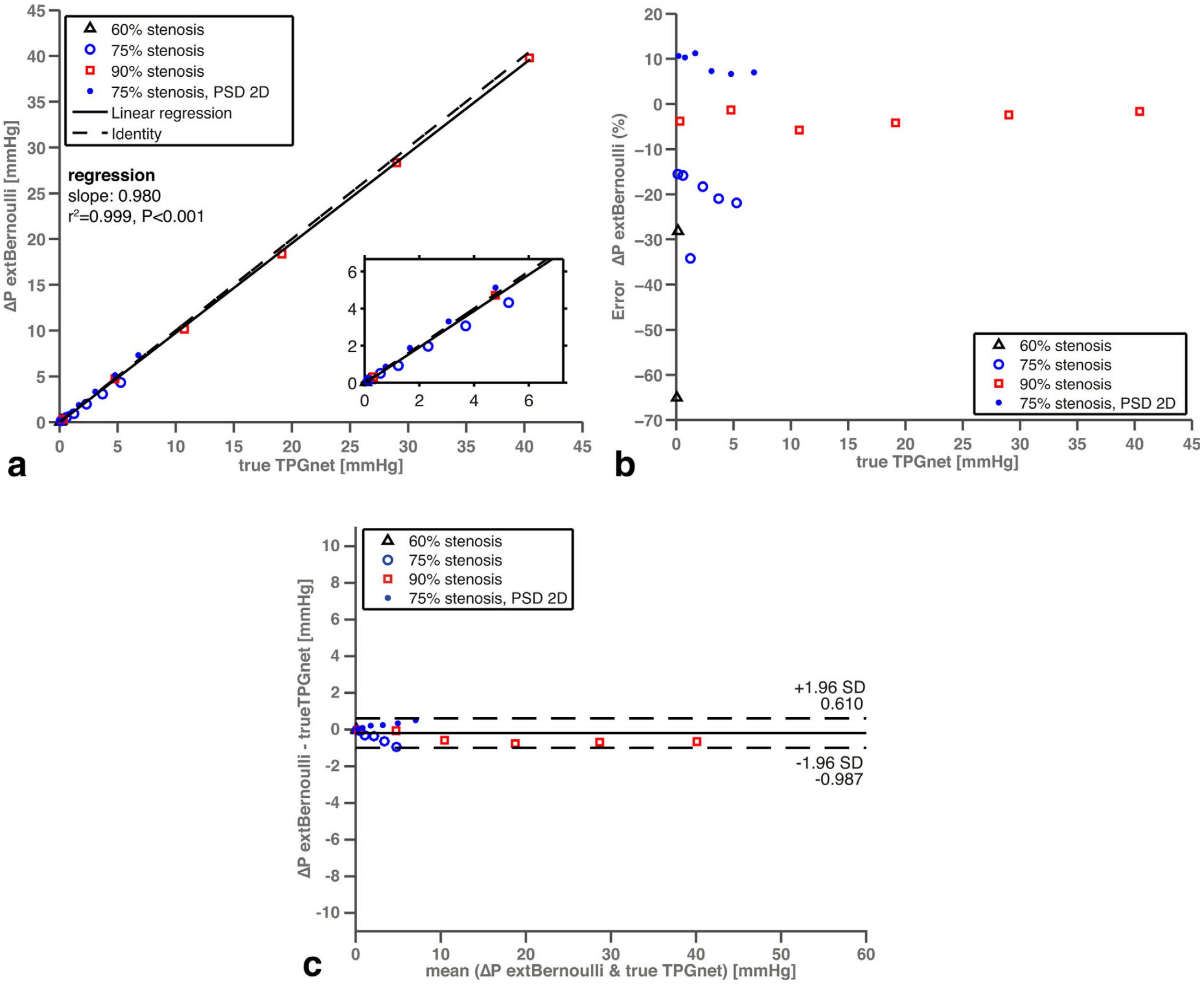

FIG. 6. Pressure gradient estimates using the extended Bernoulli equation. **a**: Correlation between the estimated pressure gradient $\Delta P_{extBernoulli}$ and the true TPG_{net}, obtained from the LES solution. An isotropic voxel size of 1 mm was considered. The solid line represents the linear regression line and the dotted line the identity. The regression line was computed including the whole TPG_{net} interval. **b**: Percentage error between the estimated pressure gradient $\Delta P_{extBernoulli}$ and the true TPG_{net}. **c**: Bland-Altman plot of $\Delta P_{extBernoulli}$ versus true TPG_{net}. The solid line is the mean bias and the dashed lines represent the ± 1.96 standard deviation (SD) lines. The different symbols indicate different geometries (size of the stenosis and presence of poststenotic dilation). For a specific geometry, increasing pressure gradients correspond to increasing Reynolds numbers.

The dependence of $\Delta P_{PPE\max}$ on resolution is depicted in Figure 7d. Resolution had a minor influence on the estimation for voxel sizes of 1 and 1.5 mm. For these resolutions, the average differences between the true $TPG_{\max}$ and $\Delta P_{PPE\max}$ were 5.8% and 10.9%, respectively. More severe underestimation was found at 2 mm resolution (average difference 31.2%), especially for the largest pressure gradients.

The relationship between the estimations of the total TKE and the true TPG_{net} for 1 mm resolution is shown in Figure 8a. For the complete set of geometries, the coefficient of determination was $r^2 = 0.756$ and the slope of the regression line 0.057 ($P < 0.001$). For a given geometry, the total TKE showed a very strong linear relationship with TPG_{net}. The coefficients of determination for the geometries represented in Figure 8a were: 0.998 for 75% stenosis without poststenotic dilation, 0.998 for 90% stenosis and 0.999 for 75% stenosis with poststenotic dilation. The slope of the regression lines for these cases was 0.132, 0.063, and 0.288, respectively, with a P-value lower than 0.001 in all cases.

There was an overall good agreement between the estimated total TKE and the reference value obtained from the LES data (Fig. 8b), which did only slightly depend on resolution for the voxel sizes considered in this study. A slight underestimation was observed for the highest TKE values, which decreased for increasing voxel sizes. The average differences between the reference and the estimated total TKE for spatial resolutions of 1, 1.5, and 2 mm were 11.3%, 8.1%, and 2%, respectively.

The correlation between $\dot{E}_{loss\ viscous}$ and the true TPG_{net} is depicted in Figures 9a,b. When $\dot{E}_{loss\ viscous}$ was computed over the entire volume (Fig. 9a), the

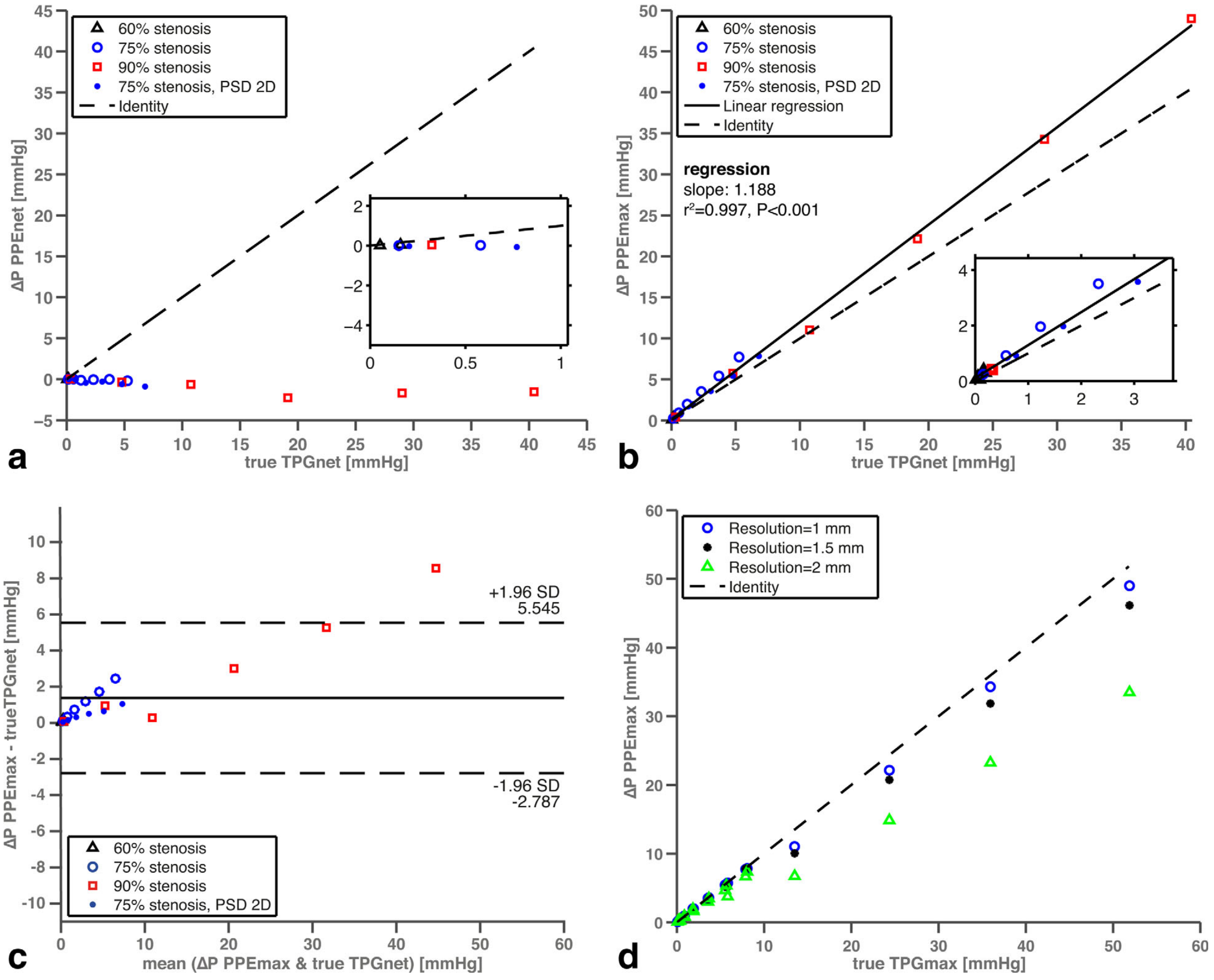

FIG. 7. Pressure gradient estimates using the PPE and dependence of $\Delta P_{PPE\max}$ on spatial resolution. **a**: Correlation between the estimated net transstenotic pressure gradient ΔP_{PPEnet} and the true $\mathrm{TPG}_{\mathrm{net}}$ value obtained from the LES solution. **b**: Correlation between the estimated maximum pressure gradient $\Delta P_{PPE\max}$ and the true value of $\mathrm{TPG}_{\mathrm{net}}$ from the LES solution. An isotropic voxel size of 1 mm was considered. The dotted line represents the identity. In B, the solid line represents the regression line, which was computed including the whole data set. **c**: Bland-Altman plot of $\Delta \mathrm{P}_{PPE\max}$ versus true $\mathrm{TPG}_{\mathrm{net}}$. The solid line is the mean bias and the dashed lines represent the ± 1.96 standard deviation (SD) lines. The different symbols indicate different geometries (size of the stenosis and presence of post-stenotic dilation). For a specific geometry, increasing pressure gradients correspond to increasing Reynolds numbers. **d**: Estimations of $\Delta P_{PPE\max}$ for three different voxel sizes: 1, 1.5, and 2 mm. The vertical axes show the estimated $\Delta P_{PPE\max}$ and the horizontal axes show the true $\mathrm{TPG}_{\max}$, derived from the LES data. The dotted line represents the identity.

relationship between both parameters was characterized by a strong linear relationship for a given geometry, but a weaker relationship when all geometries were considered. The coefficients of determination for the different geometries were: 0.934 for 75% stenotic area reduction and no poststenotic dilation, 0.965 for 90% stenotic area reduction and 0.973 for 75% stenotic area reduction and poststenotic dilation. The corresponding slopes of the linear regression lines were: 0.813, 0.047, and 0.403, with $P < 0.001$. Excluding dissipation at near wall voxels (Fig. 9b), the coefficients of determination for the given geometries were 0.776, 0.903, and 0.966, respectively, and the slopes of the linear regression lines 0.069, 0.022, and 0.076 ($P < 0.001$). Considering all geometries, the coefficient of determination between the true $\mathrm{TPG}_{\mathrm{net}}$ and $\dot{E}_{loss}$ computed from dissipation in the whole volume was $r^2 = 0.068$ and the slope of the regression line 0.029 ($P = 0.266$). If dissipation at voxels near the wall was omitted, the coefficient of determination was $r^2 = 0.776$ and the slope of the regression line 0.021 ($P < 0.001$).

Figures 9c,d show the estimations of $\dot{E}_{loss\ viscous}$ for the different voxel sizes (1, 1.5, and 2 mm) as a function of the true $\dot{E}_{loss\ viscous}$. Either considering dissipation in the entire volume (Fig. 9c) or neglecting the near wall voxels (Fig. 9d), there is poor agreement between the estimated and the actual values, with increasing underestimation of $\dot{E}_{loss\ viscous}$ values as resolution decreases. When viscous dissipation was integrated over the whole volume, the average difference between the reference and the estimated $\dot{E}_{loss\ viscous}$ for voxel sizes of 1, 1.5, and 2 mm were 68%, 87%, and 91% respectively. Neglecting

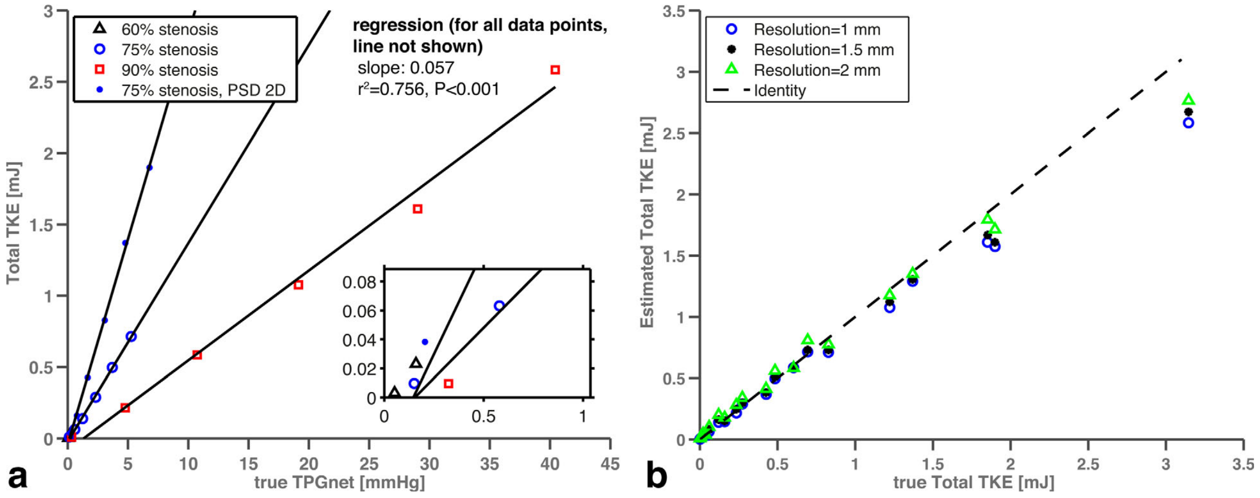

FIG. 8. Relation between total TKE and TPG_{net} and dependence of total TKE on spatial resolution. **a**: Relationship between the total TKE and the TPG_{net} values obtained from the LES solution. The results correspond to an isotropic voxel size of 1 mm. Linear regression analysis was performed for each data subset corresponding to a specific geometry, except the geometry with 60% stenotic area reduction. The solid lines represent the linear regression lines, computed for each data subset. The different symbols indicate different geometries (size of the stenosis and presence of poststenotic dilation). For a specific geometry, increasing pressure gradients correspond to increasing Reynolds numbers. **b**: Estimations of the total TKE for three different voxel sizes: 1, 1.5, and 2 mm. The vertical axes show the estimated total TKE and the horizontal axes show the true total TKE, derived from the LES solution. The dotted line represents the identity line.

dissipation at the wall region, the average differences were 54%, 67%, and 75%.

DISCUSSION

This study investigated the relationship between current 4D flow MRI-derived pressure and energy loss parameters and TPG_{net} using numerical simulations in stenotic geometries.

Several parameters overestimated or were not linearly related to actual TPG_{net} and/or depended on spatial resolution. TPG_{net} estimated with both the simplified and the extended Bernoulli equation showed a very strong linear relationship with the actual TPG_{net}. However, as expected, the simplified Bernoulli equation overestimated TPG_{net} for the whole range of pressure gradients considered in the study (0.05–40.4 mmHg), especially for low TPG_{net} values and geometries susceptible to pressure recovery (Fig. 5b). In general, the extended Bernoulli equation compensated for pressure recovery and performed better than the simplified Bernoulli equation. Some errors were still present, however, mainly for low TPG_{net} (Fig. 6b). Estimations of TPG_{net} using the PPE were approximately zero in the entire pressure interval (Fig. 7a), while TPG_{max} estimations were accurate and comparable to the values obtained with the simplified Bernoulli equation. Total TKE and viscous dissipation showed a very strong linear relationship with TPG_{net} for each geometry (Figs. 8a, 9a). However, viscous dissipation was severely underestimated and resolution dependent for all spatial resolutions included in the study (Figs. 9c,d).

The results from our computational study regarding the simplified Bernoulli equation agree well with previous in vitro and in vivo studies, which reported an overestimation of TPG_{net} when compared with catheter-based measurements (6,7,9). Such overestimation was more relevant for a higher $\text{EOA}/\text{A}_{\text{A}}$ ratio (i.e., patients with smaller aortas or less significant stenosis). This also agrees with our results, which indicate increased percentage errors for geometries with lower cross-sectional area reduction (increased EOA) and absence of poststenotic dilation. In agreement with previous studies (1,6,7), we found that the extended Bernoulli equation improved the estimation of TPG_{net}, although moderate to high underestimation (up to 65%) was present at low degrees of stenosis. However, it should be noted that the strong performance of the extended Bernoulli equation might be biased by the employed phantom geometry. The geometry consisted of a straight circular pipe and temporal terms were negligible because the flow was steady. This represents a best-case scenario for the application of the extended Bernoulli equation, which assumes a circular EOA and aortic area and negligible acceleration terms (10,16,39). Under conditions that violate these assumptions, the accuracy of the method to predict pressure recovery might decrease. Furthermore, the equation is susceptible to errors in the estimation of the peak velocity and the EOA, which will increase in vivo due to, for instance, the presence of noise.

Estimations of TPG_{net} using the PPE indicate the inability of this approach to compute irreversible pressure loss, because the mean velocities used as an input to the Navier-Stokes equations do not account for energy dissipation due to turbulence. Applying the time-averaged Navier-Stokes equations, which include the Reynolds shear stresses, might extend the pressure calculations to turbulent flow, thereby allowing estimation of the net transstenotic pressure gradient. However, in vivo measurement of the Reynolds shear stresses is still challenging (40). TPG_{max}, on the other hand, can be

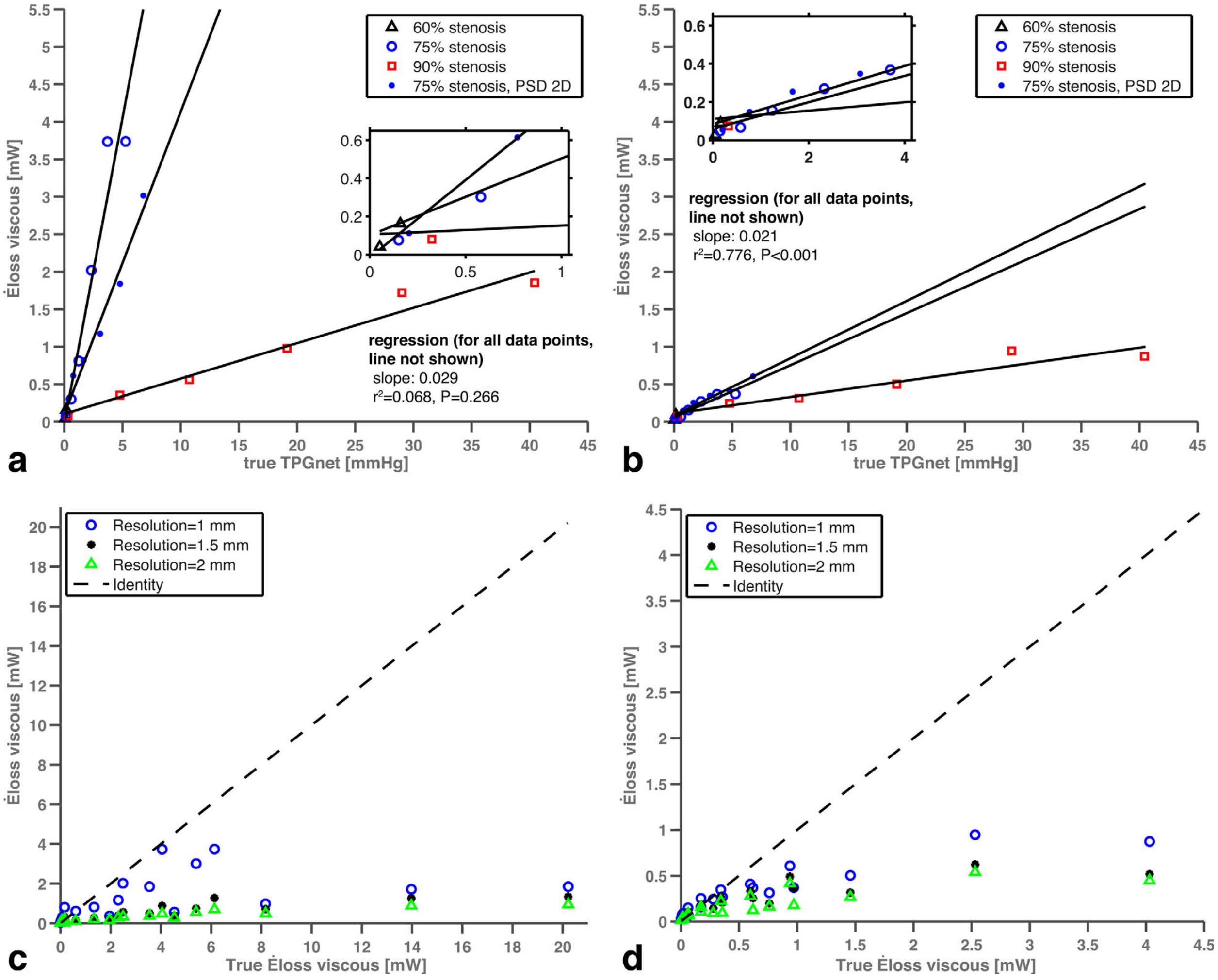

FIG. 9. Relation between the viscous energy loss rate $\dot{E}_{loss\ viscous}$ and TPG$_{net}$ and dependence of $\dot{E}_{loss\ viscous}$ on spatial resolution. a,b: Relationship between $\dot{E}_{loss\ viscous}$ and the TPG$_{net}$ values obtained from the LES solution. **a**: Viscous dissipation over the entire volume is considered. **b**: Viscous dissipation at near wall voxels is not included. An isotropic voxel size of 1 mm was considered. Linear regression analysis was performed for each data subset corresponding to a specific geometry, except the one with 60% stenotic area reduction. The solid lines represent the linear regression lines, computed for each data subset. The different symbols indicate different geometries (size of the stenosis and presence of poststenotic dilation). For a specific geometry, increasing pressure gradients correspond to increasing Reynolds numbers. **c,d**: Estimations of $\dot{E}_{loss\ viscous}$ for three different voxel sizes: 1, 1.5, and 2 mm. Estimations in (c) include viscous dissipation over the whole volume, while in (d) dissipation at near wall voxels is excluded. The vertical axes show the estimated viscous dissipation and the horizontal axes show the true viscous dissipation, computed from the LES data. The dotted line represents the identity line.

accurately computed using the PPE, as flow is laminar upstream from the vena contracta of the flow jet.

In computing TPG$_{max}$, the results from the PPE were comparable to those from the Bernoulli equation. However, our results indicate that the PPE would underestimate TPG$_{max}$ for moderate and high pressure gradients (TPG$_{max}$ > 10 mmHg) and spatial resolution lower than 1.5 mm (Fig. 7d). At these resolutions, the velocity gradients are underestimated due to partial volume effects. Applying the simplified Bernoulli equation may help overcome this issue, because errors in the estimation of peak velocity due to spatial resolution were very low (<0.37%). On the other hand, the PPE is not based on assumptions regarding flow patterns and valve and outflow tract geometries, thus could be more useful than the simplified Bernoulli equation in handling complex vessel geometries. Furthermore, it also considers the velocity proximal to the stenosis, which is not accounted for in the simplified Bernoulli equation. In our study, distal velocities had relatively low values (less than 0.43 m/s), but in cases where the distal velocity is higher (> 1 m/s) overestimation using the simplified Bernoulli approach could increase further (39).

For a given geometry, a very strong linear relationship exists between the total TKE and TPG$_{net}$ (Fig. 8a). When considering the complete set of geometries, a strong linear relationship ($r^2 = 0.756$) was found between total TKE and TPG$_{net.}$ However, the results indicate that the flow rate, the EOA and the size of the poststenotic dilation influence the total TKE, which in turn contributes to the net transstenotic pressure gradient. This agrees well with fluid mechanics theory regarding energy loss in aortic stenosis and previous work on TKE-based pressure loss estimation with MRI (4,41). TKE was accurately obtained, with an underestimation lower than 11.3%, for all resolutions included in the study. Nevertheless, it appears that for higher TKE values the accuracy of the method increases with increasing voxel sizes.

The relation between the viscous energy loss rate and TPG_{net} also depends on the geometry of the stenosis and the poststenotic dilation (Figs. 9a,b). A poor linear relationship ($r^2 = 0.068$) with TPG_{net} was seen when dissipation in the vicinity of the wall was included in the calculations. Viscous energy loss is a laminar estimate of dissipation, thus it is not surprising that it performs poorly in models that contain a significant amount of turbulence. Omitting dissipation at near wall voxels seems to neglect the effect of a poststenotic dilation (Fig. 9b), but the linear relationship between viscous dissipation rate and TPG_{net} is much higher in this case ($r^2 = 0.776$). Estimates of viscous energy loss rates were, in general, underestimated. In fact, viscous dissipation values above 4 mW could not be resolved for any of the voxel sizes used in the study (Figs. 9c,d).

Barker et al (16) postulated a correlation between total TKE and viscous dissipation. We found a very strong correlation ($r^2 = 0.918$) between these parameters when estimated directly from the LES data and when the whole flow domain was considered (thus including near-wall dissipation). A relation between viscous dissipation and turbulence seems reasonable, because the high jet velocity gradients that contribute to viscous dissipation often precede turbulence (42). However, these losses are conceptually different and cannot be seen as interchangeable. Losses due to turbulence are higher than viscous dissipation losses (38) and occur mainly downstream from the stenosis, while viscous dissipation mostly occurs at the wall and in the shear layer of the jet. These differences can be exemplified by the effect of a poststenotic dilation. The presence of a poststenotic dilation increases pressure loss. However, for the same degree of stenosis (75%), viscous dissipation is higher in the absence of poststenotic dilation, because losses at voxels near the wall are higher in this case due to a larger velocity gradient. The turbulent losses for the same stenosis degree are higher when a poststenotic dilation exists, as this geometry results in an increased Reynolds number, which promotes turbulence. Due to the inaccuracy of MR-based estimation of viscous dissipation, the correlation was much lower when the MR-based estimations were considered. For example, for a voxel size of 1 mm, the correlation between MR-estimated total TKE and viscous dissipation was $r^2 = 0.524$.

The number of voxels across the stenosis in the geometry with 90% area reduction at 1mm resolution was only five in our study. This may cause underestimation of the velocity gradients in the radial direction, specially the derivatives of the axial velocity component ($\partial v_z/\partial x$, $\partial v_z/\partial y$), leading to estimation errors in the viscous dissipation. Pressure differences along the centerline using the PPE will probably be less affected by underestimation of these velocity gradients, because they are mainly determined by the velocity gradient in the axial direction $\partial v_z/\partial z$. Errors in viscous dissipation at the stenosis site are, however, not critical for the computation of this parameter, as most dissipation occurs at the poststenotic region.

This study used simplified geometries and nonpulsatile flow and measurement noise was neglected. More realistic geometries would presumable mostly affect the Bernoulli and extended Bernoulli methods, as these methods estimates rely heavily on assumptions that were perfectly fulfilled in the present geometry, but seldom in a realistic geometry. For instance, the assumption of a circular EOA and aortic area will generally introduce errors, as these areas are typically oval instead of circular (20). An eccentric jet will further degrade the performance of the extended Bernoulli equation (43). Measurement noise would probably affect all estimates and especially viscous dissipation, which depends heavily on accurate gradient computation. In vivo, pulsatile flow and moving vessel walls will be present. Pulsatile flow has not been considered, as it would notably increase the complexity of the study and the presentation of the results. Also, the CFD simulations were performed using water instead of blood. This, however, does not affect the validity of our results. Because the simulations were designed to obtain Reynolds numbers in a specific range (500–6000), the flow rates would have been lowered to achieve the same Reynolds numbers if the viscosity of blood had been used instead. Assuming a Newtonian fluid is also reasonable, as non-Newtonian effects can generally be neglected in large vessels such as the aorta (44).

The transstenotic pressure gradient was used as a reference for evaluating aortic stenosis in our study, as this is the parameter used clinically. However, pressure gradients only represent irreversible pressure losses, and, therefore, increased ventricular workload, if the usable mechanical energy (i.e., potential and kinetic energy) of the system is reduced. This suggests that kinetic energy should also be considered to determine permanent, irreversible losses from the stenosis. For the geometries considered here, the net pressure drop corresponds to irreversible losses except for the geometry with poststenotic dilation for which the kinetic energy is higher downstream from the stenosis compared with the inlet.

Our results indicate that computation of the total TKE and viscous dissipation does not allow estimation of the net transstenotic pressure gradient directly, as its actual value depends on the specific geometry. We speculate that, in vivo, the variability in stenosis degree and poststenotic dilation would be lower than in our study, allowing direct estimation of the pressure gradient. This is consistent with the results from Dyverfeldt et al (13) and Barker et al (16), which reported strong correlations between these parameters and irreversible pressure losses in normal volunteers and patients with aortic stenosis with and without dilation. Moreover, the combination of TKE and viscous dissipation would be valuable in visualizing and identifying areas of energy loss in aortic disease. Further in vivo studies are needed to assess the applicability of these methods in various pathologies and their relation to ventricular workload.

CONCLUSIONS

Even for an idealized geometry and in the absence of measurement noise, several parameters for the assessment of stenosis severity were not linearly related to the irreversible pressure loss (TPG_{net}) and/or depended on spatial resolution. Viscous dissipation and TKE showed a strong linear relationship with TPG_{net} for a specific geometry, although this relationship was weaker when various different geometries were considered. While estimations of TKE were accurate and almost independent on spatial resolution, estimations of viscous dissipation were resolution dependent and can be considered inaccurate with commonly used spatial resolutions.

In the simple geometries considered here, the best estimations of TPG_{net} were obtained using the extended Bernoulli equation. However, the geometries and flow conditions used in this study are ideal for this method, and lower accuracy can, therefore, be expected in vivo.

REFERENCES

1. Garcia D, Pibarot P, Sakr F, Durand LG, Dumesnil JG. Assessment of aortic valve stenosis severity: a new index based on the energy loss concept. Circulation 2000;101:765–771.
2. Hatle L, Angelsen BA, Tromsdal A. Non-invasive assessment of aortic stenosis by Doppler ultrasound. Br Heart J 1980;43:284–292.
3. Bahlmann E, Cramariuc D, Gerdts E, Gohlke-Baerwolf C, Nienaber CA, Eriksen E, Wachtell K, Chambers J, Kuck KH, Ray S. Impact of pressure recovery on echocardiographic assessment of asymptomatic aortic stenosis: a SEAS substudy. JACC Cardiovasc Imaging 2010;3: 555–562.
4. Akins CW, Travis B, Yoganathan AP. Energy loss for evaluating heart valve performance. J Thorac Cardiovasc Surg 2008;136:820–833.
5. Garcia D, Durand LG, Pibarot P. Analytical modeling of the instantaneous pressure gradient across the aortic valve. J Biomech 2005;38: 1303–1311.
6. Baumgartner H, Stefenelli T, Niederberger J, Schima H, Maurer G. "Overestimation" of catheter gradients by Doppler ultrasound in patients with aortic stenosis: a predictable manifestation of pressure recovery. J Am Coll Cardiol 1999;33:1655–1661.
7. Garcia D, Dumesnil JG, Durand L-G, Kadem L, Pibarot P. Discrepancies between catheter and Doppler estimates of valve effective orifice area can be predicted from the pressure recovery phenomenon: practical implications with regard to quantification of aortic stenosis severity. J Am Coll Cardiol 2003;41:435–442.
8. Pibarot P, Dumesnil JG. Improving assessment of aortic stenosis. J Am Coll Cardiol 2012;60:169–180.
9. Niederberger J, Schima H, Maurer G, Baumgartner H. Importance of pressure recovery for the assessment of aortic stenosis by Doppler ultrasound. Role of aortic size, aortic valve area, and direction of the stenotic jet in vitro. Circulation 1996;94:1934–1940.
10. Voelker W, Reul H, Stelzer T, Schmidt A, Karsch K. Pressure recovery in aortic stenosis: an in vitro study in a pulsatile flow model. J Am Coll Cardiol 1992;20:1585–1593.
11. Ebbers T, Farnebäck G. Improving computation of cardiovascular relative pressure fields from velocity MRI. J Magn Reson Imaging 2009; 30:54–61.
12. Tyszka JM, Laidlaw DH, Asa JW, Silverman JM. Three-dimensional, time-resolved (4D) relative pressure mapping using magnetic resonance imaging. J Magn Reson Imaging 2000;12:321–329.
13. Dyverfeldt P, Hope MD, Tseng EE, Saloner D. Magnetic resonance measurement of turbulent kinetic energy for the estimation of irreversible pressure loss in aortic stenosis. JACC Cardiovasc Imaging 2013;6:64–71.
14. Clark C. Energy losses in flow through stenosed valves. J Biomech 1979;12:737–746.
15. Dyverfeldt P, Sigfridsson A, Kvitting J-PE, Ebbers T. Quantification of intravoxel velocity standard deviation and turbulence intensity by generalizing phase-contrast MRI. Magn Reson Med 2006;56:850–858.
16. Barker AJ, van Ooij P, Bandi K, et al. Viscous energy loss in the presence of abnormal aortic flow. Magn Reson Med 2014;72:620–628.
17. Garcia J, Capoulade R, Le Ven F, Gaillard E, Kadem L, Pibarot P, Larose E. Discrepancies between cardiovascular magnetic resonance and Doppler echocardiography in the measurement of transvalvular gradient in aortic stenosis: the effect of flow vorticity. J Cardiovasc Magn Reson 2013;15:84.
18. Bock J, Frydrychowicz A, Lorenz R, Hirtler D, Barker AJ, Johnson KM, Arnold R, Burkhardt H, Hennig J, Markl M. In vivo noninvasive 4D pressure difference mapping in the human aorta: phantom comparison and application in healthy volunteers and patients. Magn Reson Med 2011;66:1079–1088.
19. Lum D, Johnson K, Paul R, Turk A, Consigny D, Grinde J, Mistretta C, Grist T. Transstenotic pressure gradients: measurement in swine–retrospectively ECG-gated 3D Phase-Contrast MR angiography versus endovascular pressure-sensing guidewires. Radiology 2007;245:751.
20. Garcia J, Kadem L, Larose E, Clavel M-A, Pibarot P. Comparison between cardiovascular magnetic resonance and transthoracic Doppler echocardiography for the estimation of effective orifice area in aortic stenosis. J Cardiovasc Magn Reson 2011;13:25.
21. Nasiraei-Moghaddam A, Behrens G, Fatouraee N, Agarwal R, Choi ET, Amini AA. Factors affecting the accuracy of pressure measurements in vascular stenoses from phase-contrast MRI. Magn Reson Med 2004;52:300–309.
22. Venkatachari AK, Halliburton SS, Setser RM, White RD, Chatzimavroudis GP. Noninvasive quantification of fluid mechanical energy losses in the total cavopulmonary connection with magnetic resonance phase velocity mapping. Magn Reson Imaging 2007;25: 101–109.
23. Ahmed SA, Giddens DP. Velocity measurements in steady flow through axisymmetric stenoses at moderate Reynolds numbers. J Biomech 1983;16:505–507, 509–516.
24. Deshpande MD, Giddens DP. Turbulence measurements in a constricted tube. J Fluid Mech 1980;97(Pt 1):65–89.
25. Gårdhagen R, Karlsson M, Lantz J, Carlsson F. Quantifying turbulent wall shear stress in a stenosed pipe using large eddy simulation. J Biomech Eng 2010;132.
26. Gårdhagen R, Lantz J, Karlsson M, Carlsson F. Large eddy simulation of stenotic flow for wall shear stress estimation - validation and application. WSEAS Trans Biol Biomed 2011;8:86–101.
27. Lantz J, Gårdhagen R, Karlsson M. Quantifying turbulent wall shear stress in a subject specific human aorta using large eddy simulation. Med Eng Phys 2012;34:1139–1148.
28. Lantz J, Karlsson M, Ebbers T, Engvall J. Numerical and experimental assessment of turbulent kinetic energy in an aortic coarctation. J Biomech 2013;46:1851–1858.
29. Morbiducci U, Ponzini R, Rizzo G, Biancolini M, Iannaccone F, Gallo D, Redaelli A. Synthetic dataset generation for the analysis and the evaluation of image-based hemodynamics of the human aorta. Med Biol Eng Comput 2012;50:145–154.
30. Haacke E, Brown R, Thompson M, Venkatesan R. Magnetic resonance imaging. Physical principles and sequence design. New York: John Wiley & Sons; 1999.
31. Dyverfeldt P, Gårdhagen R, Sigfridsson A, Karlsson M, Ebbers T. On MRI turbulence quantification. Magn Reson Imaging 2009;27:913–922.
32. Baumgartner H, Hung J, Bermejo J, Chambers JB, Evangelista A, Griffin BP, Iung B, Otto CM, Pellikka PA, Quiñones M. Echocardiographic assessment of valve stenosis: EAE/ASE recommendations for clinical practice. Eur J Echocardiogr 2009;10:1–25.
33. Keshavarz-Motamed Z, Garcia J, Maftoon N, Bedard E, Chetaille P, Kadem L. A new approach for the evaluation of the severity of coarctation of the aorta using Doppler velocity index and effective orifice area: in vitro validation and clinical implications. J Biomech 2012;45: 1239–1245.
34. Caruthers SD, Lin SJ, Brown P, Watkins MP, Williams TA, Lehr KA, Wickline SA. Practical value of cardiac magnetic resonance imaging for clinical quantification of aortic valve stenosis: comparison with echocardiography. Circulation 2003;108:2236–2243.
35. Farnebäck G. Polynomial expansion for orientation and motion estimation. PhD Thesis, Linköping University; 2002.
36. Riesenkampff E, Fernandes JF, Meier S, Goubergrits L, Kropf S, Schubert S, Berger F, Hennemuth A, Kuehne T. Pressure fields by flow-sensitive, 4D, velocity-encoded CMR in patients with aortic coarctation. JACC Cardiovasc Imaging 2014;7:920–926.
37. Bird RB, Stewart WE, Lightfoot EN. Transport phenomena. New York: Wiley; 1960.
38. Pope SB. Turbulent flows. Cambridge: Cambridge University Press; 2000.

39. Marx GR, Allen HD. Accuracy and pitfalls of Doppler evaluation of the pressure gradient in aortic coarctation. J Ame Coll Cardiol 1986;7: 1379–1385.
40. Christopher E, Marcus A, Lars S, John E. Three-dimensional magnetic resonance velocimetry measurements of turbulence quantities in complex flow. Exp Fluids 2009;46:285–296.
41. Clark C. The fluid mechanics of aortic stenosis—I. Theory and steady flow experiments. J Biomech 1976;9:521–528.
42. Barker AJ, Staehle F, Bock J, Jung BA, Markl M. Analysis of complex cardiovascular flow with three-component acceleration-encoded MRI. Magn Reson Med 2012;67:50–61.
43. VanAuker MD, Chandra M, Shirani J, Strom JA. Jet eccentricity: a misleading source of agreement between Doppler/catheter pressure gradients in aortic stenosis. J Am Soc Echocardiogr 2001;14:853–862.
44. Ku DN. Blood flow in arteries. Ann Rev Fluid Mech 1997;29:399–434.